PHOTONICS Research

Free-space beam shaping and steering based on a silicon optical phased array

Wenbo Ren,[1,†] Qingqing Liang,[1,†] Jijun Feng,[1,2,*] Haipeng Liu,[1] Jianhua Hu,[1] Shuo Yuan,[1] Xincheng Xia,[1] Wei Jiang,[1] Qiwen Zhan,[1,4] and Heping Zeng[2,3]

[1]Shanghai Key Laboratory of Modern Optical System, Engineering Research Center of Optical Instrument and System (Ministry of Education), School of Optical-Electrical and Computer Engineering, University of Shanghai for Science and Technology, Shanghai 200093, China
[2]Chongqing Key Laboratory of Precision Optics, Chongqing Institute of East China Normal University, Chongqing 401120, China
[3]State Key Laboratory of Precision Spectroscopy, East China Normal University, Shanghai 200241, China
[4]e-mail: qwzhan@usst.edu.cn
[†]These authors contributed equally to this work.
*Corresponding author: fjijun@usst.edu.cn

Received 2 May 2023; revised 7 September 2023; accepted 30 September 2023; posted 2 October 2023 (Doc. ID 494546); published 24 November 2023

In this study, we present a method for free-space beam shaping and steering based on a silicon optical phased array, which addresses the theoretical limitation of traditional bulk optics. We theoretically analyze the beam propagation properties with changes in the applied phase. Different beam profiles can be shaped by varying the phase combination, while a high-order quasi-Bessel beam can be generated with a cubic change to the phase modulation. The simulated results are validated further experimentally, and they match one another well. Beam steering can be achieved with a field of view as large as 140°, which has potential benefits for practical applications. The presented method is expected to have broad application prospects for optical communications, free-space optical interconnects, and light detection and ranging.

https://doi.org/10.1364/PRJ.494546

1. INTRODUCTION

Laser beam shaping and steering have recently gained significant attention owing to their ability to generate unique field profiles such as vortex beams [1–3], Airy beams [4,5], and Bessel beams [6–8]. Bessel beams have the advantages such as excellent non-diffraction characteristics and parallel manipulation ability, making them suitable for various applications including multi-plane and multi-particle optical guidance and capture [9–11], microscopy for scattering reduction and field depth increase [12–14], enhancement of free-electron laser gain [15], medical coherence imaging [16], all-optical switching [17], and so forth. Additionally, Bessel beams find their application in optical manipulation of microtubule arrays for flow cytometry [18], encoding in free-space optical communication [19], optical drilling based on dynamic beam mixing [20], and preparing self-written waveguides and helical fibers through photo-polymerization [21]. Furthermore, high-order Bessel beams can be utilized for atomic guidance due to their non-diffraction properties with a minimum radius of the center around the same order as the incident wavelength [22].

Traditional beam-shaping techniques typically rely on some bulk optics elements, such as a phase mask, which can be modulated by a spatial light modulator (SLM) to generate a Bessel beam, and focused by a spherical lens in free space [18–21]. However, SLMs often have a limited resolution in phase discretization, and may not be ideal for miniaturization and high-density integration. Compact beam shaping devices, such as metasurfaces [23–26], fiber arrays [27,28], and integrated photonics chips [29–31], have been proposed as alternatives that do not require costly assembly or complex calibration processes. However, metasurfaces often require high-precision fabrication and fine calibration, and fiber arrays can be challenging for installation and adjustment due to the specific arrangement of multiple fibers. For integrated silicon photonic chips, they may generate beams with millimeter-level or longer lengths. Recently, silicon optical phased arrays (OPAs) have gained much attention due to their compatibility with complementary metal-oxide-semiconductor (CMOS) processing, making them suitable for low-cost applications. Integrated OPAs for generating quasi-Bessel beams have been presented [31], but the shaping and steering of different beam profiles have not been thoroughly investigated, despite their unprecedented flexibility in controlling electromagnetic waves. Further research in this area could unlock new possibilities for advanced beam shaping and steering applications.

In this paper, theoretical analysis of on-chip beam shaping and steering is presented, which is further experimentally verified by using a silicon OPA. The field distributions for various

beam profiles are simulated first by varying phase combinations. Then, a silicon OPA with an aperture of 256 μm × 256 μm is fabricated and tested for different beam generation. It is observed that a linear phase change can result in the generation of an ordinary Gaussian beam, with a steering angle of about ±70°. Furthermore, a quasi-Bessel beam can be shaped using a cubic phase change combination, which exhibits a hollow center with a length of about 0.77 mm and a power full width at half maximum (FWHM) of 8.5 μm. These experimental results confirm the effectiveness of the proposed approach for on-chip beam shaping and steering by a silicon OPA.

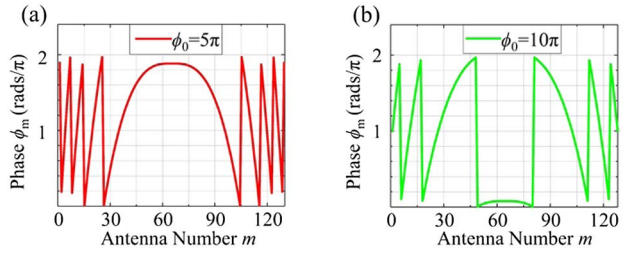

Fig. 1. Element phase distribution with (a) $\phi_0 = 5\pi$ and (b) $\phi_0 = 10\pi$, respectively.

2. THEORETICAL BEAM SHAPING AND STEERING FOR FREE SPACE

OPA is a coherent optical emission system comprising an array of antennas that are fed with controlled phases and amplitudes to generate arbitrary radiation patterns [31–36]. The near-field electric field distribution generated by the phased array can be approximately obtained by summing the electric field components of each element (I_m) in the array as

$$I(X,Y,Z) = \sum_{m=1}^{M} I_m(X,Y,Z) \approx \sum_{m=1}^{M} P_m \exp[-i(2\pi l_m/\lambda + \phi_m)]$$
$$= \sum_{m=1}^{M} \exp\left\{\frac{-4\ln 2(m - M/2 - 1/2)^2 + (MP_0)^2[-i(2\pi l_m/\lambda + \phi_m)]}{(MP_0)^2}\right\}, \quad (1)$$

where M is the total number of antennas in the array, P_m is the light amplitude of the mth antenna, P_0 is the variable initial amplitude, and $M \cdot P_0$ determines the FWHM of the amplitude curve. Here, ϕ_m is the phase applied to the mth antenna, which can be encoded modulo 2π, l_m is the distance between the coordinate point and the mth antenna, and λ is the input wavelength.

Applying the axicon-like element phase distribution of bulk optics on the basis of amplitude, different shape of light beam can be generated in the near field, and the nth-order axicon phase can be obtained by the following formula [31]:

$$\phi_m = \phi_0 \frac{-|a(m - M/2 - 1/2)|^n + M/2 - 1/2}{M/2 - 1}. \quad (2)$$

Here, a is the array factor that affects the far-field interference pattern of the beam, and ϕ_0 is a variable initial phase. To explore the influence of phased array elements on the beam under the application of different variable phase parameters, representative variable phase parameters are selected. The variable phase parameter ϕ_0 can be taken as 5π, 10π, and 20π, respectively. For example, the corresponding phase distribution curves for 5π and 10π are shown in Figs. 1(a) and 1(b), respectively. When n is 0 with variable phase parameter $\phi_0 = 0$ and amplitude parameter $P_0 = 1$, a Gaussian beam will be generated as shown in Fig. 2(a). When n is 1, 2, or 3 with the variable phase parameter ϕ_0 of 5π and amplitude parameter P_0 of 1, the field distributions generated by the simulated one-dimensional free space beam array are shown in Figs. 2(b)–2(d).

From the simulated field distribution in Fig. 2(b), it can be seen that the array can generate a quasi-Bessel beam, which has been demonstrated before [31] and will not be discussed here. When $n = 2$, OPA can also generate a convergent beam [Fig. 2(c)]. Due to its slight similarity with the Gaussian beam, it will also be skipped for simplicity. With a cubic phase change combination of $n = 3$, a high-order quasi-Bessel beam can be generated, as presented in Fig. 2(d). This configuration results in the formation of a hollow-core central cavity [28]. The beam has a good propagation stability and can be used for large particle trapping, facilitating its application in optical microscopy [37] and the treatment of material surfaces [38]. For further comparison, the corresponding transverse light field distributions at the position $Z = 4$ mm are also shown in Figs. 2(e)-2(h), respectively. The beam profile variation from the Gaussian shape to hollow-core central cavity can be clearly seen.

The simulated field distributions with different initial phase and amplitude for the cubic phase change combination ($n = 3$) are shown in Fig. 3. As can be seen from Figs. 3(a)–3(c), the size and position of the hollow-core beam will be affected by changing the initial phase. With increase of the initial phase, the hollow core size will decrease, with its position closer to the array surface. With the changing initial amplitude as shown in Fig. 3(d), the contrast ratio will be reduced with a half unit amplitude, resulting in a degraded performance compared to that in Fig. 3(b). Therefore, adjusting the initial phase and amplitude can help to design the beam shape. The power FWHM and beam length of the hollow-core are usually adopted for the beam quality evaluation. Here, power FWHM is a full width calculated on the plane where the power of the central beam is half-maximally enhanced. The beam length is defined as the point above the array where the central beam is approximately disabled. The simulated power FWHM and beam length corresponding to Figs. 3(a)–3(d) are listed in Table 1.

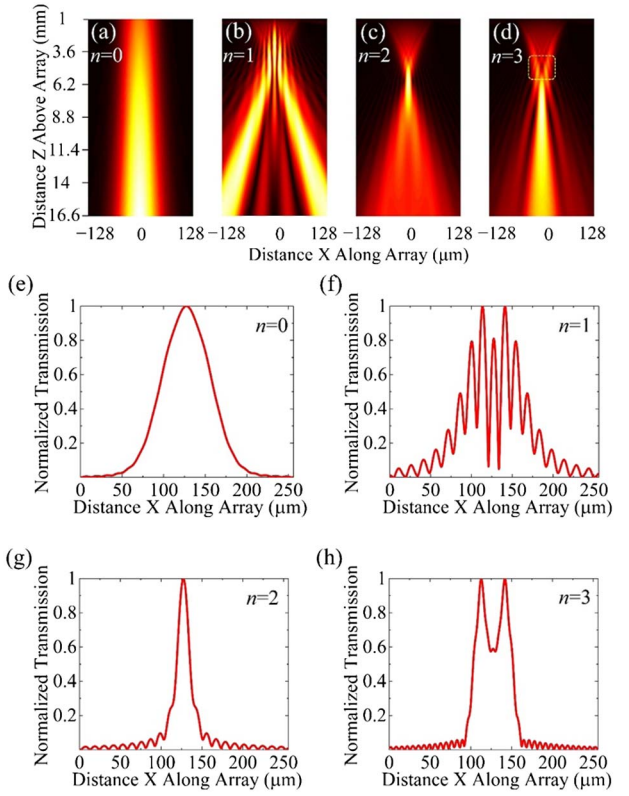

Fig. 2. Simulated near-field distribution above the array for (a) a Gaussian beam with $n = 0$, $\phi_0 = 0$ and $P_0 = 1$, (b) $n = 1$ with $a = 1$, $\phi_0 = 5\pi$, and $P_0 = 1$, (c) $n = 2$ with $a = 0.1$, $\phi_0 = 5\pi$, and $P_0 = 1$, and (d) $n = 3$ with a = 0.05, $\phi_0 = 5\pi$, and $P_0 = 1$, where the dotted rectangle shows a hollow-core central cavity. (e), (f), (g), and (h) are the corresponding simulated curves of the transverse light field at $Z = 4$ mm when $n = 0$, 1, 2, and 3, respectively.

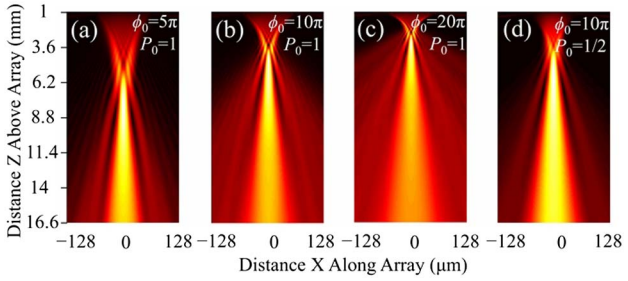

Fig. 3. Simulated near-field distribution above the array for the cubic phase change combination with (a) $\phi_0 = 5\pi$ and $P_0 = 1$, (b) $\phi_0 = 10\pi$ and $P_0 = 1$, (c) $\phi_0 = 20\pi$ and $P_0 = 1$, and (d) $\phi_0 = 10\pi$ and $P_0 = 1/2$.

Table 1. Simulated Power FWHM and Beam Length for the OPA with Cubic Phase Change Combination

Parameters	Power FWHM (μm)	Beam Length (mm)
$\phi_0 = 5\pi$ and $P_0 = 1$	9.728	1.271
$\phi_0 = 10\pi$ and $P_0 = 1$	6.336	0.624
$\phi_0 = 20\pi$ and $P_0 = 1$	4.672	0.472
$\phi_0 = 10\pi$ and $P_0 = 1/2$	6.464	0.651

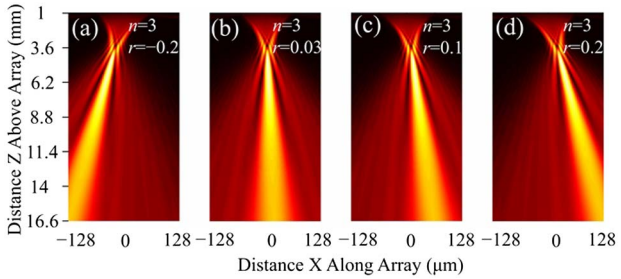

Fig. 4. Simulated steering results for a quasi-Bessel beam with a cubic phase change combination and varying r of (a) −0.2, (b) 0.03, (c) 0.1, and (d) 0.2, respectively.

Silicon OPAs can be programmed to steer the generated optical field. A linear change of the phase combination can realize the beam deflection, which can be expressed as

$$\phi_m = rm + b + \phi_0 \frac{-|a(m - M/2 - 1/2)|^n + M/2 - 1/2}{M/2 - 1}. \quad (3)$$

Here, r is the steering coefficient, which can determine the deflection angle, and b is the steering constant depending on the antenna aperture. For the presented high-order quasi-Bessel beam with a cubic phase change combination, the beam steering results can be simulated with varying r. The field distribution at different deflection angle with $b = 1.4$ is shown in Fig. 4. A large beam deflection angle of ±70° can be realized as shown in Figs. 4(a) and 4(d). Compared with the traditional beam-shaping technique based on bulk optics elements, OPA can achieve more flexible, accurate, and faster beam steering.

3. EXPERIMENTAL RESULTS

As a proof of concept, the OPA chip was fabricated by ultraviolet (UV) lithography with a standard commercial CMOS facility. The antenna aperture size is 256 μm × 256 μm. The OPA architecture used here is based on a splitting tree structure, as shown in Fig. 5(a). The input light couples into the waveguide via end-coupling, and is split into 128 channels

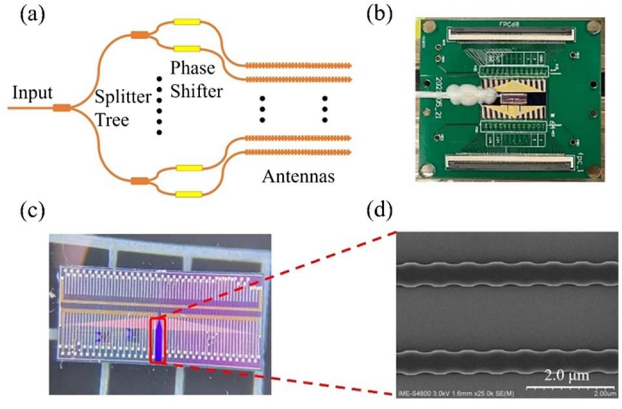

Fig. 5. (a) Schematic diagram of silicon OPA with (b) and (c) for the microscope image of the packaged device and OPA chip, respectively. (d) SEM image of the grating waveguide antenna.

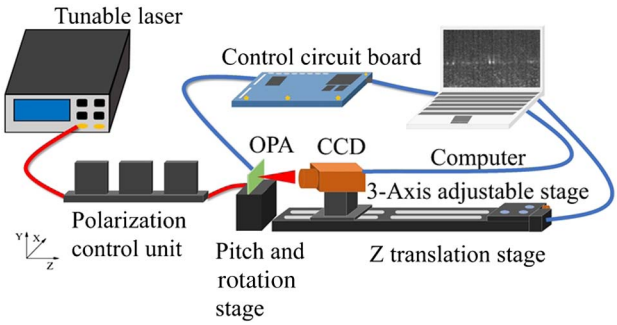

Fig. 6. Schematic illustration of the experimental setup for the characterization of beam shaping and steering.

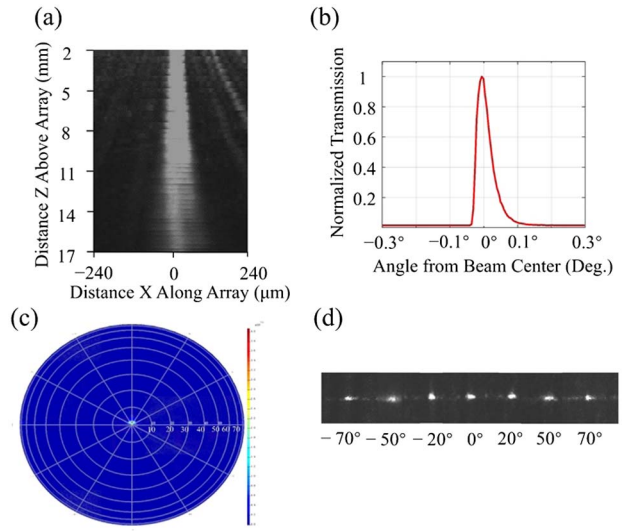

Fig. 7. (a) Measured cross-sectional intensity distribution of OPA along the exit Z direction in the free space for Gaussian beam with $n = 0$. (b) Cross-sectional profile of the recorded light spot, with (c) and (d) for the steering result of simulation and experiment with a deflection angle of about ±70°, respectively.

by a cascaded 1 × 2 MMI splitter. A micro-heater-based phase shifter is integrated on each channel for phase modulation, which consists of TiN with a size of 5 μm × 200 μm and a resistance of about 1 kΩ and can achieve a π-phase shifter with an 18.7 mW power consumption. Light in each channel exits into free space via the sidewall-grating-based waveguide antenna, and it interferes in the far field region. Figure 5(b) shows the packaged chip, with Fig. 5(c) for the microscope image of the fabricated chip. Figure 5(d) presents the scanning electron microscope (SEM) image of the sidewall grating waveguide antenna, which has a period of 650 nm and a duty cycle of 0.5. The sidewall grating antenna used here can help to increase the light emission length and improve the roundness of the far-field pattern. In addition, temperature is also a key factor affecting the beam shaping performance. Here, a thermoelectric cooler (TEC) was adopted in the experiment to reduce the impact of temperature.

The schematic diagram of the experimental device for beam shaping and control characteristics is shown in Fig. 6. A tunable laser was used as the light source at a 1550 nm wavelength, and it was connected with a polarization controller and coupled into the waveguide through a packaged lensed fiber. The output light from OPA was emitted to the free space and monitored by a charge coupled device (CCD), which was monitored by a computer. The computer then generated a required voltage combination for the control circuit, which was applied to the phase shifter above the waveguide, and the phase would change correspondingly. Through this feedback unit, a particle swarm optimization algorithm was adopted for the compensation of initial phase error caused by random non-uniformity of waveguides, which can converge more easily to an optimal solution with a fixed number of paths than the adjacent sampling principal component analysis method [39,40]. Then the specific beam profile could be generated with the desired phase combination. The CCD was mounted on a linear electric stage, to record the field distribution along the exit Z direction in the free space.

For the Gaussian beam case with $n = 0$, it is the normal beam steering configuration, and the recorded light intensity along the exit direction is shown in Fig. 7(a). A sidelobe suppression ratio of larger than 10 dB can be realized. The divergence angle is about 0.1°, with the cross-sectional beam profile shown in Fig. 7(b). A large steering angle of about ±70° can be achieved by a linear change of the waveguide phase, with the theoretical and experimental results shown in Figs. 7(c) and 7(d), respectively. When the input optical power is about 10 mW, the output power of the main lobe is about 15.3 μW, resulting in a total loss of about 28 dB, which is slightly high and still needs further optimization. However, the current chip can still be used for the beam-shaping and steering demonstration. Figures 8(a)–8(d) verify a quasi-Bessel beam generation with $n = 1$. The corresponding beam

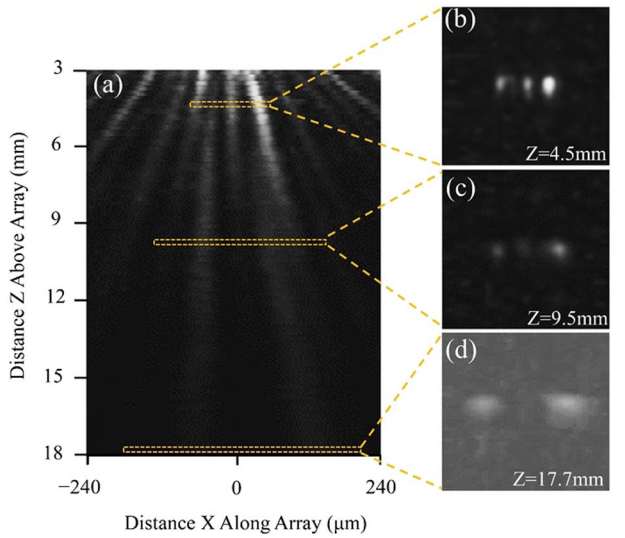

Fig. 8. (a) Measured cross-sectional intensity above the chip for a quasi-Bessel beam generation ($n = 1$, $\phi_0 = 5\pi$ and $P_0 = 1$), with top-down intensity (b) within the quasi-Bessel region of the emitted beam ($Z = 4.5$ mm), (c) at the edge of the quasi-Bessel region ($Z = 9.5$ mm), and (d) after breakdown of the quasi-Bessel region ($Z = 17.7$ mm).

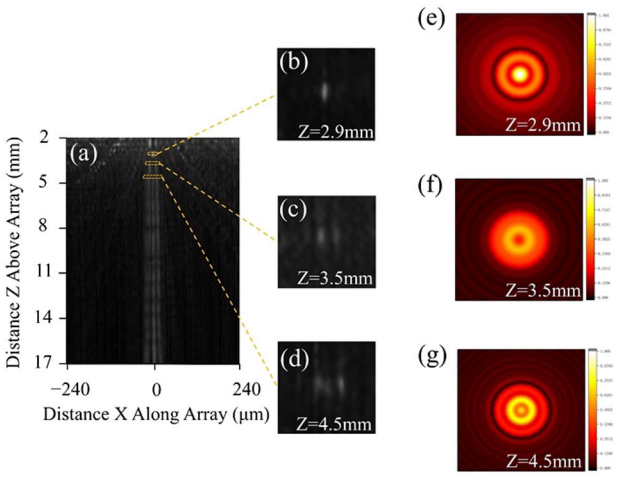

Fig. 9. (a) Measured cross-sectional intensity above the chip for a high-order quasi-Bessel beam generation ($n = 3$, $\phi_0 = 10\pi$, and $P_0 = 1$), with top-down intensity (b) near the converged region ($Z = 2.9$ mm), (c) at the hollow-core region ($Z = 3.5$ mm), and (d) at the split hollow core region ($Z = 4.5$ mm). (e)–(g) are the simulated light field distributions at the corresponding region.

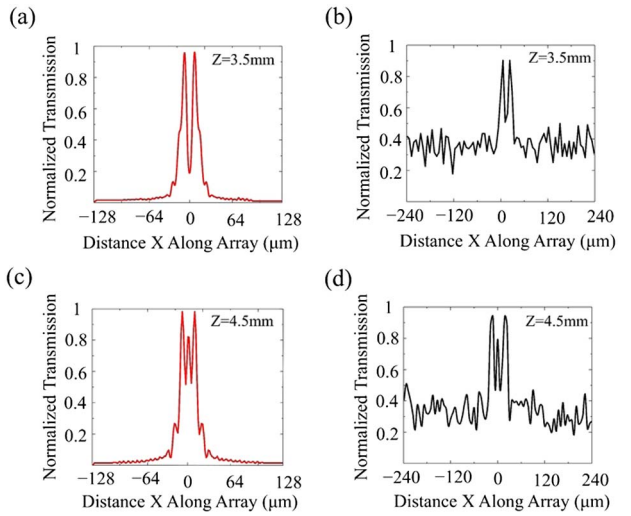

Fig. 10. Normalized intensity distribution of the simulated high-order quasi-Bessel beam above the chip at Z position of (a) 3.5 mm and (c) 4.5 mm, with (b) and (d) for the corresponding measured results, respectively.

length is approximately 10.6 mm, comparable with the simulated value of 12.4 mm. The difference may come from the waveguide fabrication errors, thermal crosstalk, and free-space stray light of the device itself.

For the cubic phase change combination with ϕ_0 of 10π and $P_0 = 1$, the corresponding cross-sectional intensity distribution is shown in Fig. 9, and a hollow-core beam can be generated. As can be seen from Fig. 9(a), a power FWHM of ~8.5 μm was measured along the hollow-core beam, matching the simulated value of 6.34 μm. Furthermore, a hollow core beam length of ~0.77 mm was measured, near the simulated value of 0.62 mm. The corresponding top-down views of light intensity distribution at different position above the chip are shown in Figs. 9(b)–9(d), which are near the converged region ($Z = 2.9$ mm), the hollow-core region ($Z = 3.5$ mm), and the split hollow core region ($Z = 4.5$ mm) of the emitted beam, respectively. The measured results are similar to the simulated one in Fig. 3(b). The simulated light intensity distributions at the corresponding position are shown in Figs. 9(e)–9(g), respectively.

It should be noted that the theoretical results [Figs. 9(e)–9(g)] are slightly similar to the ideal higher-order Bessel beam, and thus a quasi-Bessel beam can be generated here. However, there is still some difference, which may be due to the diffraction effects originating from the chip, as well as the phase error caused by random non-uniformity of waveguides. Furthermore, the imaging quality of the infrared camera is constrained by its 20 μm resolution. The amplitude of each channel may also be slightly different, which would influence the final light field distribution, although the amplitude of each channel cannot be adjusted here. By adding a Mach–Zehnder interferometer unit to control the output light amplitude of each channel, more complex light fields can be generated. Furthermore, the simulated and measured cross-sectional intensity distributions for the emitted beam at the hollow-core region ($Z = 3.5$ mm), as well as the split hollow core region ($Z = 4.5$ mm) are presented in Fig. 10. They can coincide well with each other, despite of some noisy background. Note that a larger-scale integrated OPA has been applied for the Bessel–Gaussian beam generation [41], which can be used for long-range sensing. In addition, femtosecond-laser direct writing of three-dimensional phase plates can also generate Bessel beams efficiently and quickly [42]. Here, we systematically summarized and experimentally verified the potential beam shaping and steering with silicon OPA. The presented method provides a new version for high-order quasi-Bessel beam generation, which can be expected to have broad application prospects.

4. CONCLUSION

To summarize, we have successfully demonstrated a silicon OPA for free-space beam shaping and steering. Through detailed analysis of the phase and amplitude distribution, a variety of special free-space beams can be generated, including but not limited to Gaussian and quasi-Bessel beams. Our results show that a Gaussian beam with a divergence angle of approximately 0.1° can be achieved, with a steering angle of about ±70°. Furthermore, a high-order quasi-Bessel beam can be generated with an cubic phase change combination, exhibiting a hollow length of ~0.77 mm and an FWHM of about 8.5 μm. The effectiveness of the proposed approach for on-chip beam shaping and steering can open the door to applications from optical communications to atomic guidance.

Funding. National Key Research and Development Program of China (2022YFE0107400); National Natural Science Foundation of China (11727812, 11774235, 11904232, 11933005, 61705130); Science and Technology

Commission of Shanghai Municipality (23010503600, 23530730500); Program for Professor of Special Appointment (Eastern Scholar) at Shanghai Institutions of Higher Learning (GZ2020015).

Author Contributions. Conceptualization, J.F., Q.Z. and H.Z.; methodology, J.F., Q.L., Q.Z. and H.Z.; validation, S.Y., H.L. and J.H; formal analysis, J.F., Q.Z, W.R. and H.L.; investigation, J.F., W.R. and Q.Z.; resources, J.F.; data curation, J.F., W.R. and Q.L.; writing—original draft preparation, W.R. and Q.L.; writing—review and editing, J.F., Q.Z., H.L., J.W., X.X. and H.Z.; supervision, J.F., Q.Z. and H.Z.; project administration, J.F.; funding acquisition, J.F. All authors have read and accepted the published version of the manuscript.

Disclosures. The authors declare no conflicts of interest.

Data Availability. Data underlying the results presented in this paper are not publicly available at this time but may be obtained from the authors upon reasonable request.

REFERENCES

1. J. Cheng, C. Wan, and Q. Zhan, "Generalized spiral transformation for high-resolution sorting of vortex modes," Opt. Lett. **48**, 1762–1765 (2023).
2. A. Chong, C. Wan, J. Chen, and Q. Zhan, "Generation of spatiotemporal optical vortices with controllable transverse orbital angular momentum," Nat. Photonics **14**, 350–354 (2020).
3. C. Wan, J. Chen, A. Chong, and Q. Zhan, "Generation of ultrafast spatiotemporal wave packet embedded with time-varying orbital angular momentum," Sci. Bull. **65**, 1334–1336 (2020).
4. C. Xu, H. Hu, Y. Liu, and D. Deng, "Radially polarized symmetric Airy beam," Opt. Lett. **45**, 1451–1454 (2020).
5. Z. A. Kichi and S. G. Sabouri, "Multiple Airy beam generation by a digital micro mirror device," Opt. Express **30**, 23025–23034 (2022).
6. A. Müller, M. C. Wapler, and U. Wallrabe, "Segmented Bessel beams," Opt. Express **25**, 22640–22647 (2017).
7. Q. Fontaine, H. Hu, S. Pigeon, T. Bienaimé, E. Wu, E. Giacobino, A. Bramati, and Q. Glorieux, "Attenuation-free non-diffracting Bessel beams," Opt. Express **27**, 30067–30080 (2019).
8. O. C. Vicente and C. Caloz, "Bessel beams: a unified and extended perspective," Optica **8**, 451–457 (2021).
9. V. Garcés-Chávez, D. McGloin, H. Melville, W. Sibbett, and K. Dholakia, "Simultaneous micromanipulation in multiple planes using a self-reconstructing light beam," Nature **419**, 145–147 (2002).
10. A. Kritzinger, A. Forbes, and P. B. C. Forbes, "Optical trapping and fluorescence control with vectorial structured light," Sci. Rep. **12**, 17690 (2022).
11. M. Mohammadnezhad, S. S. Abdulkareem, and A. Hassanzadeh, "Creation of rotating spiral structures using interfering Bessel beams for optical manipulation," Opt. Lett. **47**, 4024–4027 (2022).
12. F. O. Fahrbach, P. Simon, and A. Rohrbach, "Microscopy with self-reconstructing beams," Nat. Photonics **4**, 780–785 (2010).
13. T. Meinert and A. Rohrbach, "Light-sheet microscopy with length-adaptive Bessel beams," Biomed. Opt. Express **10**, 670–681 (2019).
14. H. He, Y. X. Ren, R. K. Y. Chan, W. L. So, H. K. Fok, C. S. W. Lai, K. K. Tsia, and K. K. Y. Wong, "Background-free volumetric two-photon microscopy by side-lobes-cancelled Bessel beam," IEEE J. Sel. Top. Quantum Electron. **27**, 6801307 (2021).
15. G. Pan, M. Xun, X. Chen, Z. Zhao, Y. Sun, J. Zhou, and D. Wu, "High-compactness Bessel beam emitters based on vertical-cavity surface-emitting lasers," IEEE Trans. Electron Devices **69**, 2508–2513 (2022).
16. A. F. Valle and J. D. Seelig, "Two-photon Bessel beam tomography for fast volume imaging," Opt. Express **27**, 12147–12162 (2019).
17. Y. Chai, N. Marsal, and D. Wolfersberger, "Three-dimensional all-optical switching using a single diffracting Bessel beam," Phys. Rev. Appl. **17**, 064063 (2022).
18. L. Yang, S. Ji, K. Xie, W. Du, B. Liu, Y. Hu, J. Li, G. Zhao, D. Wu, W. Huang, S. Liu, H. Jiang, and J. Chu, "High efficiency fabrication of complex microtube arrays by scanning focused femtosecond laser Bessel beam for trapping/releasing biological cells," Opt. Express **25**, 8144–8157 (2017).
19. S. Li and J. Wang, "Adaptive free-space optical communications through turbulence using self-healing Bessel beams," Sci. Rep. **7**, 43233 (2017).
20. G. Kontenis, D. Gailevičius, N. Jiménez, and K. Staliunas, "Optical drills by dynamic high-order Bessel beam mixing," Phys. Rev. Appl. **17**, 034059 (2022).
21. Y. Arita, J. Lee, H. Kawaguchi, R. Matsuo, K. Miyamoto, K. Dholakia, and T. Omatsu, "Photopolymerization with high-order Bessel light beams," Opt. Lett. **45**, 4080–4083 (2020).
22. K. D. J. Arlt, "Generation of high-order Bessel beams by use of an axicon," Opt. Commun. **177**, 297–301 (2000).
23. M. Khorasaninejad, W. T. Chen, R. C. Devlin, J. Oh, A. Y. Zhu, and F. Capasso, "Metalenses at visible wavelengths: diffraction-limited focusing and subwavelength resolution imaging," Science **352**, 1190–1194 (2016).
24. Y. Fan, B. Cluzel, M. Petit, X. L. Roux, A. Lupu, and A. Lustrac, "2D waveguided Bessel beam generated using integrated metasurface-based plasmonic axicon," ACS Appl. Mater. Interfaces **12**, 21114–21119 (2020).
25. J. Yang, T. K. Hakala, and A. T. Friberg, "Generation of arbitrary vector Bessel beams on higher-order Poincare spheres with an all-dielectric metasurface," Phys. Rev. A **106**, 023520 (2022).
26. W. Chen, M. Khorasaninejad, A. Y. Zhu, J. Oh, R. C. Devlin, A. Zaidi, and F. Capasso, "Generation of wavelength-independent subwavelength Bessel beams using metasurfaces," Light Sci. Appl. **6**, e16259 (2017).
27. I. V. A. K. Reddy, A. Bertoncini, and C. Liberale, "3D-printed fiber-based zeroth- and high-order bessel beam generator," Optica **9**, 645–651 (2022).
28. M. Lahrberg, F. Tsige Dullo, and B. S. Ahluwalia, "Photonic-chip based free space beam shaping and steering for advanced optical microscopy application," OSA Contin. **3**, 359–378 (2020).
29. W. Hao, J. Wang, and L. Chen, "Compact broadband silicon-integrated Airy beam emitter," Opt. Lett. **46**, 4084–4087 (2021).
30. Z. Fang, R. Chen, A. Ryou, and A. Majumdar, "1D self-healing beams in integrated silicon photonics," ACS Photon. **8**, 2139–2147 (2021).
31. J. Notaros, C. V. Poulton, M. J. Byrd, M. Raval, and M. R. Watts, "Integrated optical phased arrays for quasi-Bessel-beam generation," Opt. Lett. **42**, 3510–3513 (2017).
32. T. Fukui, R. Tanomura, K. Komatsu, D. Yamashita, S. Takahashi, Y. Nakano, and T. Tanemura, "Non-redundant optical phased array," Optica **8**, 1350–1358 (2021).
33. J. Notaros, C. V. Poulton, M. Raval, and M. R. Watts, "Near-field-focusing integrated optical phased arrays," J. Lightwave Technol. **36**, 5912–5920 (2018).
34. Y. Li, B. Chen, Q. Na, Q. Xie, M. Tao, L. Zhang, Z. Zhi, Y. Li, X. Liu, X. Luo, G. Lo, F. Gao, X. Li, and J. Song, "Wide-steering-angle high-resolution optical phased array," Photon. Res. **9**, 2511–2518 (2021).
35. A. Kazemian, P. Wang, Y. Zhuang, and Y. Yi, "Optimization of the silicon-based aperiodic optical phased array antenna," Opt. Lett. **46**, 801–804 (2021).
36. A. Raptakis, L. Gounaridis, M. Weigel, M. Kleinert, M. Georgiopoulos, E. Mylonas, P. Groumas, C. Tsokos, N. Keil, H. Avramopoulos, and C. Kouloumentas, "2D optical phased arrays for laser beam steering based on 3D polymer photonic integrated circuits," J. Lightwave Technol. **39**, 6509–6523 (2021).
37. Y. Zhang, W. Dong, Y. Zhang, X. Tang, G. Xiao, Z. Liu, J. Zhang, J. Yang, and L. Yuan, "All-fiber hollow Bessel-like beam for large-size particle trap," J. Lightwave Technol. **39**, 3291–3296 (2021).
38. J. Xu, K. Pan, and D. Zhao, "Random sources generating hollow array beams," Opt. Express **28**, 16772–16781 (2020).

39. Y. Huang, K. Wang, Q. Yan, Y. Wang, X. Wang, H. Liu, J. Feng, F. Zhang, Z. Feng, and G. A. Siviloglou, "Universal dimension reduced phase compensation algorithm for an optical phased array," Opt. Lett. **47**, 2871–2874 (2022).
40. S. Cheng, H. Lu, X. J. Lei, and Y. H. Shi, "A quarter century of particle swarm optimization," Complex Intell. Syst. **4**, 227–239 (2018).
41. Z. Zhi, Q. Na, Q. Xie, B. Chen, Y. Li, X. Liu, X. Li, L. Wang, G. Lo, and J. Song, "On-chip generation of Bessel–Gaussian beam via concentrically distributed grating arrays for long-range sensing," Light Sci. Appl. **12**, 92 (2023).
42. J. Wang, C. Cai, K. Wang, and J. Wang, "Generation of Bessel beams via femtosecond direct laser writing 3D phase plates," Opt. Lett. **47**, 5766–5769 (2022).